

Study of Electron Transport Layer-Free and Hole Transport Layer-Free Inverted Perovskite Solar Cells

Adva Shpatz Dayan and Lioz Etgar*

The selective contacts in perovskite solar cells play a major role in solar cell (SC) performance and optimization. Herein, the inverted architecture is focused on, where systematically the electron transport layer (ETL) and the hole transport layer (HTL) from the SC structure are eliminated. Three main architectures of the SCs are studied: a fully inverted structure, an ETL-free structure, and a HTL-free structure. Cathodoluminescence and photoluminescence are measured on various architectures, revealing the electron and hole injection efficiency from the perovskite to selective contacts. Moreover, surface voltage spectroscopy shows the type and the band-edge transition of these layers. Finally, the photovoltaic (PV) performance of different SCs shows that eliminating the HTL is most critical for PV performance, compared with ETL-free and fully inverted SC configurations. Current–voltage hysteresis curves prove that efficient selective contacts are essential to eliminate this phenomenon. Measuring the ideality factor shows that the dominant mechanism in ETL-free SCs is surface recombination, whereas in the other cases, it is Shockley–Reed–Hall recombination. This work provides knowledge about the functionality of methylammonium lead iodide as an electron conductor and as a hole conductor.

1. Introduction

The power conversion efficiency (PCE) of perovskite-based solar cells (SCs) has increased dramatically in the last 10 years to more than 25%, competing well with other exciting SC technologies.^[1–3] Organic–inorganic perovskite has unique and superior properties such as broad absorption, a long diffusion length, and it can be composed of a solution that makes it very suitable to function as a light harvester in SCs.^[4–7,8]

Perovskite solar cells (PSCs) have three main architectures: 1) a planar structure; 2) a mesoporous structure; and 3) an inverted structure.^[9–11] Type (1) has the structure ITO/FTO, ETL (compact TiO₂ or SnO₂), a perovskite layer, HTL (S2,2,7,7-tetrakis-(*N,N*-di-methoxyphenylamine)-9,9-bifluorene (spiro-OMeTAD) or poly-triarylamine (PTAA), or poly(3-hexylthiophene-2,5-diyl) (P3HT)) and metal contact. Type (2) has layers

relatively similar to type (1), with the addition of a mesoporous TiO₂ layer, that is, ITO/FTO, electron transport layer (ETL), mesoporous TiO₂, hole transport layer (HTL), and metal contact. Type (3) is an inverted structure, which means that the HTL is first deposited, followed by the perovskite, and then the ETL. The possible HTL in this case is PEDOT:PSS or self-assembled monolayer (SAM, MeO-2PACz, [2-(3,6-dimethoxy-9-*H*-carbazol-9-yl)ethyl] phosphonic acid), and the ETL can be phenyl-C61-butyric acid methyl ester (PCBM).^[12–16]


An additional possible SC function is to eliminate the HTL or the ETL. In these cases, the perovskite has to function simultaneously as a light harvester and a hole conductor or an electron conductor. The HTL-free PSC was first reported in 2012,^[17] Elimination of the HTL has several advantages, such as avoiding oxidation, simpler SC fabrication, and reduced cost.

Nevertheless, it is not obvious to simply eliminate an important layer from the SC, as it will harm the performance, even though a PCE of 11.6% was reported.^[18,19]

In addition to HTL-free cells, there are a few reports on ETL-free cells,^[20–22] whereas for inverted structures, there are even fewer reports,^[23] mainly due to the importance of this layer to the PV performance. One of the main obstacles of ETL-free cells (for an inverted structure) lies in the direct contact of the perovskite with the metal contact (due to the elimination of the ETL). Perovskite tends to oxidize from the environment and therefore a passivation layer is created between the perovskite and the metal contact, which harms the PV performance.^[24–26] In contrast, it can also prevent degradation of the perovskite layer.^[27,28] The most common materials that can be self-assembled with high electron mobility include fullerene derivatives,^[29] carboxyl groups,^[30] pyridine,^[31] and low-dimensional perovskite.^[32] Since 2018, bathocuproin (BCP) has been used as a passivation layer in inverted structure cells.^[33,34] It was found that BCP passivates the defects in the perovskite layer in addition to enhancing the perovskite's resistivity to moisture without altering its structure.

Three main factors need to be taken into account when developing HTL- or ETL-free PSCs. The first one is related to the difference in the energy levels between the perovskite and the metal contact or the FTO glass. With ETL-free or HTL-free cells, this energy difference is larger than that in the case of one of the common architectures discussed earlier. This energy difference can

A. Shpatz Dayan, L. Etgar
Institute of Chemistry
Casali Center for Applied Chemistry
The Hebrew University of Jerusalem
Jerusalem 91904, Israel
E-mail: lioz.etgar@mail.huji.ac.il

 The ORCID identification number(s) for the author(s) of this article can be found under <https://doi.org/10.1002/solr.202100578>.

DOI: 10.1002/solr.202100578

be a source for recombination centers and other possible resistances. The second point is related to the electronic properties of each material. HTL usually involves aromatic rings that enhance hole mobility, whereas ETL is usually a metal oxide, such as TiO_2 or ZnO , which encourages the injection of electrons into the anode. The third point is the solvent engineering of the different layers in the SC. When one layer is eliminated, it is important to ensure that the solvent of one layer will not harm the layer beneath it. In this work, we studied the effect of electron and hole transport layers in inverted perovskite-based SCs. This study investigated the optical and physical properties as well as the photovoltaic (PV) performance of several combinations of ETL-free, HTL-free, and fully inverted perovskite SCs.

Figure 1 shows the structures of the SCs studied in this work. Figure 1a shows an inverted structure with PCBM as the ETL and PEDOT:PSS as the HTL. The other two cases are an ETL-free cell (Figure 1b) and a HTL-free cell (Figure 1c).

2. Results and Discussion

Figure 2a shows the absorbance spectra of the perovskite (i.e., MAPbI_3) used in the three SC architectures; the E_g value is 1.57 eV and it is similar for the three cases. We chose MAPbI_3 to reduce any possibility of phase segregation or other effects that can influence the device performance other than the selective contacts studied here.^[35]

To study the luminescence of the SCs' architecture, we measured the cathodoluminescence (CL) (Figure 2b) and photoluminescence (PL) (Figure 2c). Regarding the CL measurement, the excitation was carried out using an electron beam of 5 V, which penetrates deeply into the SC layers. Figure S1, Supporting Information, shows a simulation of the penetration depth for the three cases; as shown, in all three cases, the beam penetrates through all the layers. However, the PL measurement is based on excitation by a light source, where the signal detection is mainly

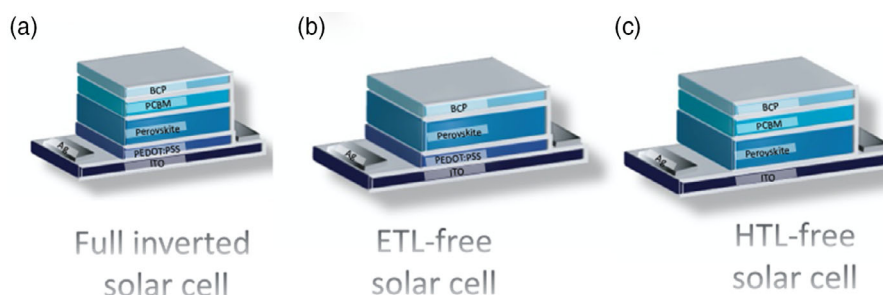


Figure 1. Schematic illustration of the three architectures studied in this work. a) An inverted PSC; b) an ETL-free SC; and c) an HTL-free SC.

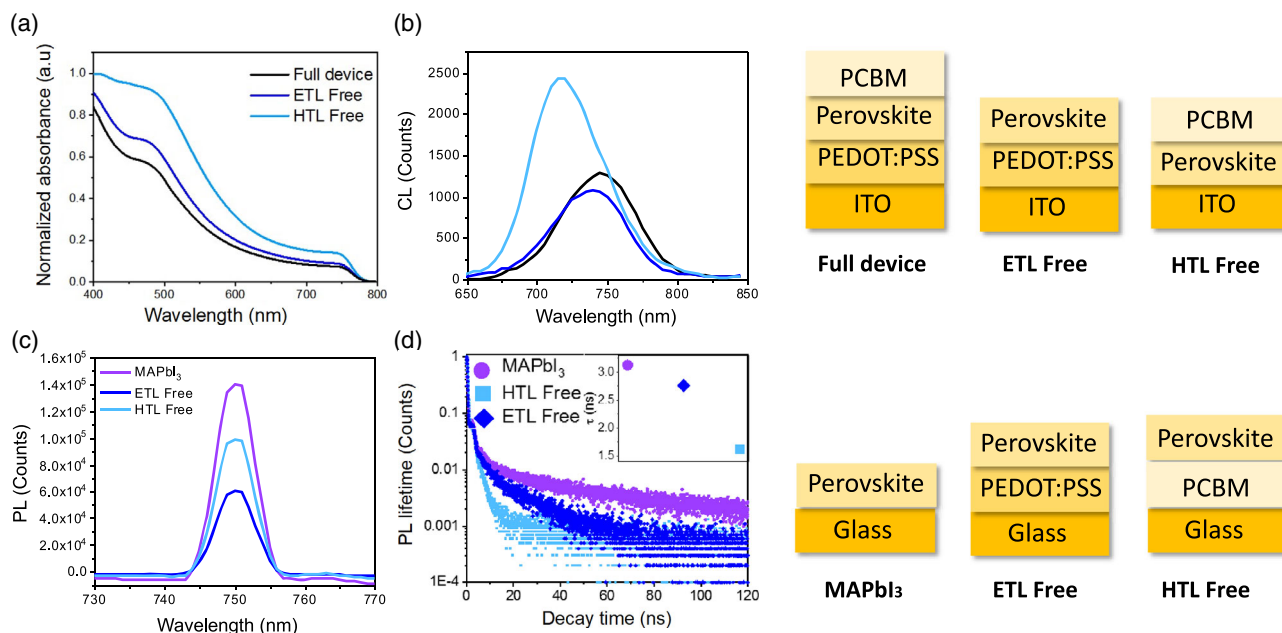


Figure 2. a) Absorbance spectra for the three different architectures: a fully inverted SC, an ETL-free SC, and an HTL-free SC. b) CL spectra for the three architectures. Right: A schematic illustration of the CL-measured samples. c) PL spectra for HTL-free and ETL-free SCs, and the perovskite (MAPbI_3) layer. Right: A schematic illustration of the PL-measured samples. d) PL decay for the HTL-free and ETL-free SCs and the perovskite (MAPbI_3) layer (Table S1, Supporting Information, shows the fitting parameters).

from the surface of the substrate. A schematic illustration of the samples' configuration for the PL and CL measurements is shown in the right of Figure 2.

The full width at half maximum (FWHM) of the CL measurements for the three SC structures is very similar (Figure 2b). In contrast, the peak position is blue-shifted for the HTL-free case (725 nm), compared with the ETL-free and full cells (750 and 753 nm, respectively). The CL measurements were performed on the structures, as presented in the upper right of Figure 2. The blue-shift in the CL is due to several factors, 1) the passivation of defects in MAPbI₃ by lead iodide which forms a type II structure; and^[36] 2) the passivation of the perovskite's surface by PCBM, which reduces the trapped electrons at this interface. In the case of ETL free, as there is no PCBM layer, there are more trapped electrons. Moreover the CL measurements penetrate through the entire layers of the cell (as discussed previously); as a result, in the case of full cells, the PEDOT:PSS minimizes any bulk charge recombination, while in the case of HTL-free cells, the bulk charge recombination is enhanced, which provides a blue-shift in CL.^[37]

It can be seen that with the HTL-free cells, the grain size is smaller ($\approx 0.9 \mu\text{m}$) than the grain size for ETL-free cells ($\approx 2.6 \mu\text{m}$) (Figure 3a–d). Moreover, there are more large pinholes with the HTL-free cell than with the ETL-free cell. When the perovskite is deposited on top of the HTL (PEDOT:PSS), its roughness is smaller than when the perovskite is deposited directly on a bare ITO layer, which results in larger perovskite grains.^[38,39]

The PL measurement (Figure 2c) was carried out on the samples' structure, as presented in the bottom right of Figure 2. A clear difference can be observed in the PL intensity; in the case of only perovskite on glass, there is no electron injection from the perovskite to the substrate; therefore, the radiative recombination is high. In the other two configurations, the perovskite is deposited on ETLs (PCBM, HTL-free cells) or HTLs

(PEDOT:PSS, ETL-free cells); therefore, it can indicate the electron or hole injection of the perovskite into selective contacts. As the PL intensity of the ETL-free cell is lower than that of the HTL-free cell, we can assume that with MAPbI₃, hole injection is more efficient than electron injection. To get a more general conclusion, we study another two HTLs (P3HT, CuSCN) and additional two ETLs (C₆₀, TiO₂). Figure S3, Supporting Information, shows the PL spectra of the four samples. The same trend is observed also in these cases, which lead us to the conclusion that hole injection is more efficient than electron injection in the case of MAPbI₃.

Following the CL and PL measurements, we performed PL decay measurements for the three cases on the same structure of samples as for the PL (Figure 2d). A longer electron lifetime was observed for the MAPbI₃ layer on glass, whereas the HTL-free cell displayed the shortest electron lifetime, which corresponds to 1.62 ns, suggesting more radiative recombination, which is not beneficial for SC performance, as will be seen in the PV results.

Figure 3a shows the scanning electron microscope (SEM) micrographs for HTL-free samples (Figure 3a,b) and perovskite on top of HTLs (Figure 3c,d). It is clear that the substrate on which the perovskite layer is deposited plays a major role in the morphology observed.^[40,41] Regarding the HTL-free cell, the perovskite is deposited directly on the ITO substrate, whereas for the ETL-free cell, the perovskite is deposited on the PEDOT:PSS film. This affects the grain size and the pinholes in the film, as mentioned previously. Figure S2, Supporting Information, shows the histograms of the size distributions for the two cases, where the grain sizes are bigger when deposited on top of PEDOT:PSS compared with the case when deposited directly on ITO. In addition, the morphology of the crystals also changes. Figure 3c shows a well-defined crystal with a "lego-like" pattern (which was reported previously^[42]), whereas in Figure 3b, in the case of HTL-free cells, the crystals are less well defined.

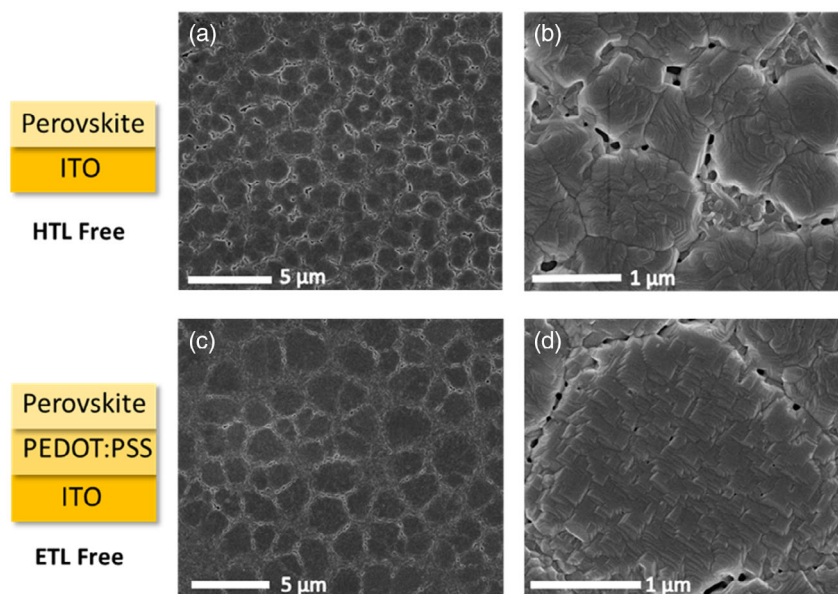


Figure 3. a,b) SEM micrographs for the HTL-free sample. c,d) SEM micrographs for the ETL-free sample.

The morphology of the perovskite deposited on other HTLs (i.e., P3HT and CuSCN) was studied, as shown in Figure S4, Supporting Information. Consistent with the previous results (Figure 3c–d), the perovskite film shows a continuous layer without pinholes when deposited on the HTLs, which further supports the difference in the perovskite layer when it is directly deposited on ITO (i.e., HTL free).

Next, surface photovoltage spectroscopy (SPV) was applied to the^[40,43] different materials used in this study. This method is based on the classical Kelvin probe technique, which measures the difference in the work function (also known as the contact potential difference [CPD]) between a metallic reference probe and a semiconductor surface.^[44] The SPV analyses of multilayer structures offer the possibility of performing contactless and nondestructive electrical and optical characterization of buried interfaces. **Figure 4a** shows the SPV measured in the dark and under white light for the different ETLs, HTLs, and perovskite cells used in this study. The Fermi level and the quasi-Fermi level can be extracted from this measurement; therefore, the type of material can be observed; PEDOT:PSS and MAPbI₃ are p-type materials, whereas PCBM and BCP are n-type materials based on the SPV measurements. This is in good agreement with the SC configurations. **Figure 4b** shows SPV measurements of a full SC where all the layers can be recognized. An increase in the

CPD results in a p-type behavior, whereas a decrease in the CPD results in an n-type material. In the different areas in the graph, this can be attributed to MAPbI₃, PCBM, and BCP. This is further supported by extracting the bandgaps (“band-edge transition”) of the different materials to be 1.5 eV for MAPbI₃, 2.1 eV for PCBM, and 3.4 eV for BCP, which are in good agreement with the bandgap calculated from the absorption measurements. (The SPV for the other architectures is shown in Figure S5, Supporting Information.) **Figure 4c** shows the energy levels’ positions based on literature values, which are in good agreement with our SPV measurements.^[45,46]

SCs based on the three architectures were fabricated to study the PV properties of each SC. **Figure 5** shows the efficiency (a), J_{SC} (b), V_{OC} (c), and fill factor (FF) (d) of the SCs. (A summary of the PV results is shown in Table S2, Supporting Information.) It can be seen that the full architecture of the SC displays the best PV parameters. However, when the ETLs or the HTLs layers are removed, the PV performance decreases. The most affected parameter is V_{oc} , which decreases from 0.88 V to 0.75 V and 0.56 V for a full SC, an ETL-free, and a HTL-free cell, respectively (Figure 5c). In addition to V_{oc} , the fill factor is also dramatically affected by the device structure, where it decreases from $\approx 67\%$ to $\approx 50\%$, which has a major effect on the efficiency of the SCs. Both the fill factor and V_{oc} are affected by the recombination process in

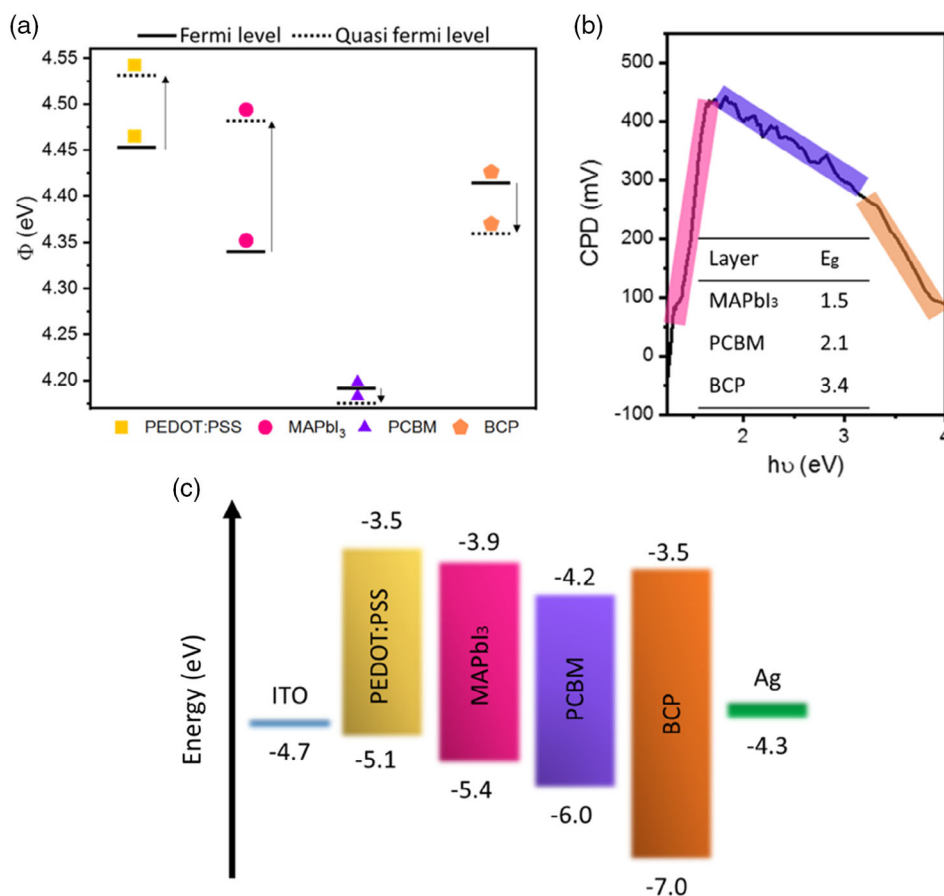


Figure 4. a) Fermi level and the quasi-Fermi level for each layer in the full SC used in this study. b) SPV spectra for the full SC. c) Energy-level diagram of the different materials used in this study (the data for the energy levels’ positions are taken from other studies^[45,46]).

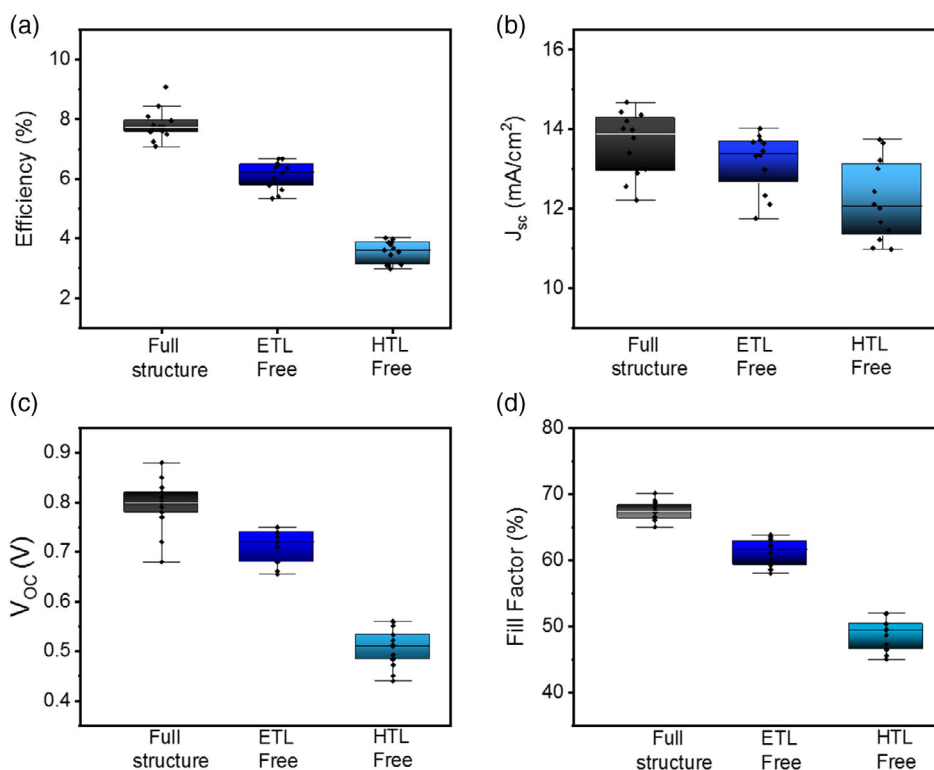


Figure 5. PV parameters for the three different architectures. a) Efficiency, b) J_{sc} , c) V_{oc} , and d) fill factor.

the cell; once the ETL or HTL layers are eliminated, there are more paths for recombination to take place. The main reasons for the reduction in the V_{oc} and FF of the cells are associated with the pinholes in the perovskite layer, as shown in the HTL-free configuration (Figure 3b), and are due to the mismatch in the energy levels, as shown in Figure 4c. Moreover an interesting observation comes from the hysteresis of the $J-V$ curves (Figure S9, Supporting Information); the inverted full SC structure shows negligible hysteresis, whereas in the case of the HTL- and ETL-free cells, the hysteresis can be clearly observed. This indicates that the selective contacts are responsible for the hysteresis in such SC configurations. The HTL and ETL layers are responsible for the extraction of the charge carriers from the cell; once these layers are eliminated from the SC, the charges cannot extract efficiently, which creates hysteresis.

The parameter that has the smallest change as a result of different SC structures is the current density (J_{sc}), as shown in Figure 5b. **Figure 6a** shows the $J-V$ curves for the different architectures, which clearly show that V_{oc} is mostly affected by the SC structure where the J_{sc} value is very similar. Figure 6d shows SEM cross section of the full SC, where all the layers can be seen.

The external quantum efficiency (EQE) spectra of the three different architectures are shown in Figure 6b. EQE measurements are based on the ratio of the number of incident photons to the number of generated charge carriers. In general, it is possible to present the total percent EQE as a multiplication of three different components, $\eta_{\text{collection efficiency}} \times \eta_{\text{injection efficiency}} \times \eta_{\text{light harvesting}}$; $\eta_{\text{collection efficiency}}$ is affected by four main properties: the absorption coefficient (α), solar spectrum, diffusion length, and depletion

region width. The most affected parameter is the width of the depletion region. This parameter can be changed with the voltage, which can reduce the collection efficiency and create a shunting effect.^[47,48] The $\eta_{\text{injection efficiency}}$ is related to the ETLs/HTLs.^[49] The quality of these layers and the energy levels' alignment affect the injection efficiency. It is known that in MAPbI₃ the electron injection time is longer than the thermalizing process.^[50] The $\eta_{\text{light harvesting}}$ efficiency is mainly related to the perovskite layer, MAPbI₃, in this case.

In this study, the light harvesting material was kept the same; therefore, it is believed that the other two factors mainly affected the EQE spectra. The most dramatic change in the EQE spectra is observed in the 620–800 nm region (green region in the graph). In this region, the HTL has the major contribution, which is related to the injection efficiency.^[51] The EQE spectra of the HTL-free cell start to decrease from 585 nm, whereas the EQE spectra of the full SC start to decrease from 740 nm; this suggests that the HTL contributes to the EQE spectra in this region. The other interesting part of the EQE spectra is related to the 300–400 nm region (yellow region in the graph). This range is commonly associated with the ETL ($\eta_{\text{collection efficiency}}$, $\eta_{\text{injection efficiency}}$).^[52] It can be observed that in the ETL-free SC the increase in the EQE is much sharper and its maximum is lower than that of the EQE spectrum of the HTL-free SC and the full SC. Finally, the integrated J_{sc} (calculated from the EQE measurement) and the J_{sc} , measured at the solar simulator, are observed in the inset of Figure 6b; the corresponding graphs are shown in Figure S6, Supporting Information. There is good agreement between both J_{sc} values.

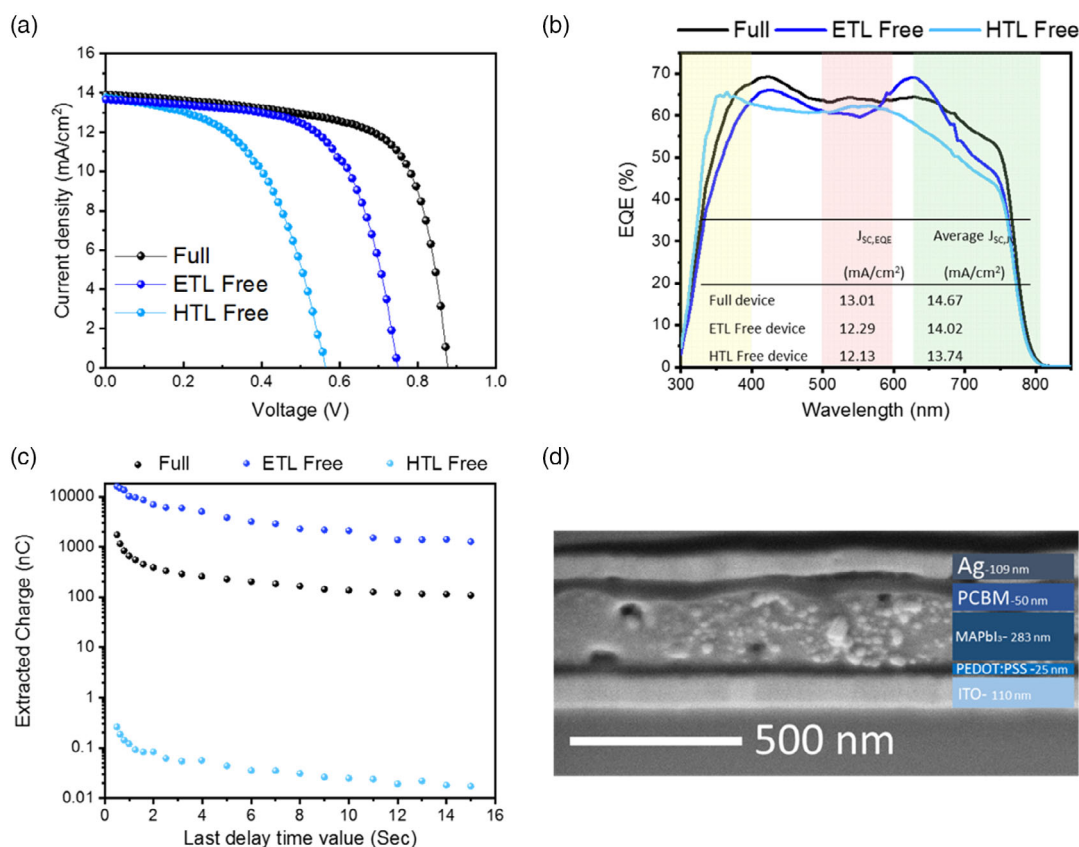


Figure 6. a) J - V curve of the champion cells of each architecture. b) EQE spectra. c) CE measurements for the three architectures. d) Cross-section SEM image of the full PSC.

Charge extraction (CE) analysis is shown in Figure 6c. This measurement can provide knowledge about the transport, trapping, and back reaction of the charges in the SC. A typical CE experiment is composed of 1) a two-second step in which the cell is discharged in the dark; 2) the cell then disconnected and illuminated for 2 s (illumination time); 3) the light that is then switched off and the system that waits a certain time called delay time. In this step, a charge recombination occurs inside the cell; and 4) The cell is reconnected and the charges which were left and do not recombine are extracted and measured. This process is repeated for different delay times, from 0.5 to 15 s. The charges collected are plotted against delay time to give insight into the lifetime of the charges after certain delay time. There is a large difference in the extracted charges in a full SC and an ETL-free SC, compared with the HTL-free SC. In both cases, the PV performance was higher than the third case of the HTL-free SC. The lowest V_{oc} value was observed in the HTL-free cell, which is associated with the recombination in this SC structure, as supported by the CE measurements. When the HTL is removed, there is direct contact between MAPbI₃ and ITO, which inhibits the hole injection. This is also in good agreement with the PL decay results, which show the shortest electron lifetime in the case of the HTL-free SC.

The current density as a function of light intensity (starting from 0.027 mW cm⁻² to 1 sun illumination) for the three architectures is shown in Figure 7a and S7, Supporting Information.

The slope is similar for the three architectures, with $\alpha \approx 1$, which indicates that these SCs do not display a space-charge effect.^[53] The dark current for these three SC structures (Figure S8, Supporting Information) shows the smallest leakage current with the full SC, whereas the highest leakage current is observed for the HTL-free cell, which is in good agreement with the PV performance. Figure 7b shows the V_{oc} as a function of light intensity; the slope of this curve indicates the ideality factor (n_{ID}). If the ideality factor is lower than 1, then the dominant mechanism is surface recombination, whereas if the ideality factor is between 1 and 2, the dominant mechanism is Shockley-Reed-Hall (SRH).^[54] In this study, the ETL-free cells received $n_{ID} = 0.89$; this suggests that surface recombination is the dominant mechanism mainly due to the direct contact of the evaporated contact with the perovskite. With the fully inverted perovskite SC and the HTL-free cell, the ideality factors are 1.34 and 1.32, respectively. The recombination mechanism in these cases is mainly related to the bulk and they behave as SRH recombination.

3. Conclusion

In this work, we studied the effect of ETLs and HTLs on the performance of inverted perovskite-based SC structures. The HTL-free cells exhibit the lowest efficiencies and PV

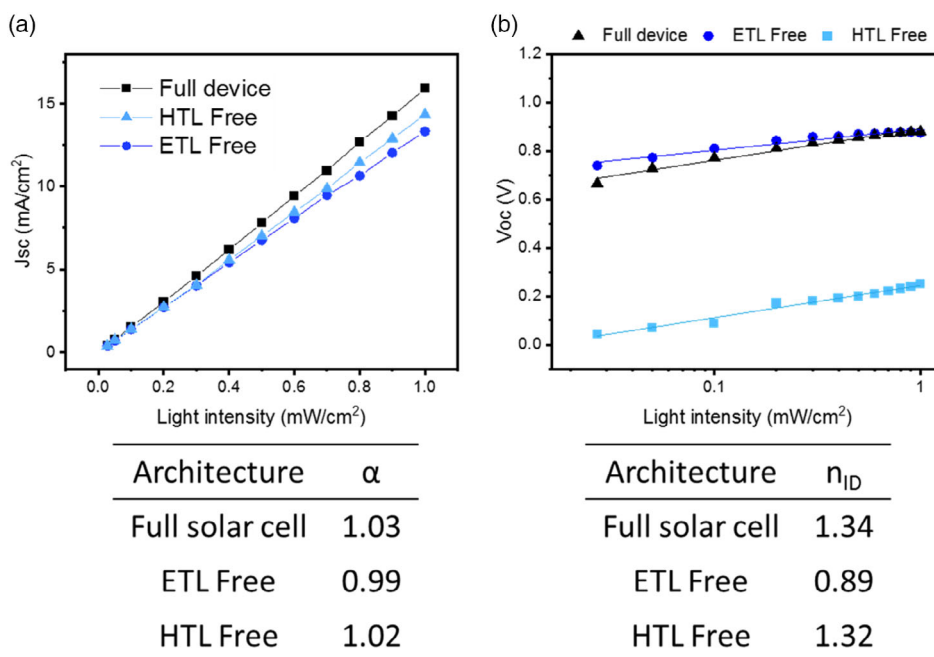


Figure 7. a) J_{sc} versus light intensity. b) V_{oc} versus light intensity.

parameters compared with the other architectures. Optical characterizations show different electron and hole injection efficiencies, which correspond with the PL lifetime between these architectures. SPV measurements reveal the material type and the quasi-Fermi-level position. ETLs and HTLs are necessary to obtain an efficient PV performance; however, their weight in obtaining efficient PV performance is not equal. It can be concluded that HTL is more critical to obtain high PV performance. As a result, it can be concluded that MAPbI₃ is more efficient as an electron conductor compared with its functionality as a hole conductor. This work provides a different view point of the MAPbI₃ perovskite properties, which is beneficial for developing highly efficient and stable PSCs.

4. Experimental Section

Device Fabrication: ITO conductive glass (12–15 Ohm) was etched by the reaction of zinc powder with HCl (37% Sigma). After etching, the glass was cleaned with 2 mL of Hellmanex III in 100 mL TDW in a sonication bath for 15 min. Then, it was cleaned with isopropanol for more than 30 min in a sonication bath. This was followed by oxygen plasma treatment (80% power, Diener). PEDOT: PSS Al 4083 (Ossila) was deposited by spin coating (7000 rpm for 60 s); then, the substrates were annealed at 140 °C for 20 min. When it cooled down to 100 °C, the substrates were inserted to the glovebox immediately. For perovskite deposition, 50 μ L of perovskite solution was dropped on the middle of the substrate, followed by a spin-coating process, with a 5 s delay time, 10 s spin at 1000 rpm, and 45 s spin at 5000 rpm. 25 s before the end of spin coating, 100 μ L of toluene was added drop wise onto the substrate. The cells were annealed at 100 °C for 45 min. Next, the PCBM film was deposited: PCBM 99% (Ossila)/chlorobenzene (sigma) (30 mg/1 mL), 100 μ L from the solution was deposited in the dynamic spin-coated solution at 2000 rpm for 35 s and annealed at 100 °C for 10 min. BCP > 99.5 purity (Ossila)/isopropanol (sigma) (1 mg/1 mL), 150 μ L from the solution was deposited in the spin-coated solution at 6000 rpm for 35 s and annealed at 75 °C for 5 min.

Finally, a 100 nm-thick silver electrode was thermally evaporated on the film under a vacuum of $\approx 10^{-7}$ Torr.

Preparation of Perovskite Solutions: The perovskite solutions were prepared in a nitrogen-filled glovebox $H_2O < 0.1$ ppm and $O_2 < 2.0$ ppm. All of the inorganic precursors were purchased from Sigma Aldrich. 0.2225 g of MAI (Greatcell) and 0.5808 g of PbI₂ (Sigma) were dissolved in 300 μ L DMSO (Sigma) and 700 μ L of gamma-butyrolactone (GBL) (Sigma). The solution was stirred and heated at 70 °C for 1 h.

Absorbance Measurements: Absorbance measurements were performed using a Jasco V-670 spectrophotometer.

CL Measurements: The measurements were taken in high-resolution SEM Sirion XL30 SFEG (ThermoFisher, former FEI). The measurements conditions were 5 kV, 5 nm spot size, 1000 \times magnification, and 2 s dwell time.

PL Measurements: PL measurements and PL lifetime were measured by HORIBA FluoroMax 4, using a light source of an ozone-free xenon arc lamp 150 W. The sample PL was detected by a photon counting detector (R928P photomultiplier tube) and a reference detector of UV-enhanced silicon photodiode. The samples were excited at a wavelength of 500 nm, slit size of 5 nm. PL lifetime was measured by 730 nm laser excitation.

The samples for the PL measurements were prepared separately for each substrate. First, microscope glass was cleaned in a sonication bath for 15 min followed by oxygen plasma treatment (80% power, Diener). For PEDOT:PSS and PCBM, the concentration, preparation, and annealing were the same like in the devices. For CuSCN layer, 0.024 g of CuSCN were dissolved in 1000 μ L dimethyl sulfide, followed by 3000 rpm in a spin coater for 30 s; annealing was for 10 min at 50 °C. For P3HT layer, 0.015 g of (poly(3-hexylthiophene-2,5-diyl) (P3HT) was dissolved in 1000 μ L toluene and mixed with 7.5 μ L of Li solution (0.058 g of Li-TFSI (bis(trifluoromethane)sulfonimide) in 500 μ L acetonitrile). Then, 7.5 μ L 4-tert-butylpyridine (TBP) was added, followed by 3000 rpm in the spin coater for 30 s. For C₆₀ layer, 0.0005 g of C₆₀ was dissolved in 1000 μ L dichloromethane, followed by 2000 rpm in the spin coater for 30 s; annealing was for 5 min at 60 °C. For m-TiO₂ nanoparticles (30-NRD, dyesol) (1:8 w/w⁻¹ in ethanol absolute) by spin coating (5000 rpm for 30 s); the annealing temperature was 325 °C for 10 min, 450 °C for 10 min, and 500 °C for 30 min. Following the HTL or ETL deposition, the perovskite was deposited as follows: 40 μ L of perovskite solution was dropped

on the middle of the substrate, followed by a spin-coating process, with a 5 s delay time, 10 s spin at 1000 rpm, and 45 s spin at 5000 rpm. 25 s before the end of the spin coating, 100 μ L of toluene was added drop wise onto the substrate. The substrates were annealed at 100 °C for 45 min.

Surface Photovoltage Spectroscopy: SPV and work function were performed using the SKP5050-SPS040 system. The CPD between the sample and the vibrating tip was measured by the Kelvin probe technique. The substrates were measured in a Faraday cage under air environment. The Fermi level was measured in the dark and the quasi-Fermi level was measured under a 150 W quartz tungsten halogen lamp. For surface photovoltage spectroscopy (SPS) measurements, the samples were illuminated with a 150 W quartz tungsten halogen lamp. Before the measurement, samples were stabilized with a tip for about 90 min. The scan direction was from long-to-short wavelength. The WF was calculated according to: $WF_{\text{substrate}} = WF_{\text{gold tip}} - CPD_{(\text{tip-substrate})}$.

Ultrahigh Resolution Scanning Electron Microscopy (UHR-SEM) and Focused Ion Beam (FIB): The sample was placed inside a FEI Helios Nano Lab 460F1 and excavated using a focused gallium-ion beam to expose the layered structure. The layered stack was tilted to 52.0° and imaged on a separate holder. The images conditions were 2 kV, 0.1 nA, and the detector was through the lens detector (TLD).

PV Characterization: PV measurements were performed using a Newport system, composed of an Oriel I–V test station using an Oriel Sol3A simulator. The solar simulator was class AAA for spectral performance, uniformity of irradiance, and temporal stability. The solar simulator was equipped with a 450 W xenon lamp. The output power was adjusted to match AM1. The spectrally matched classic cations were IEC60904-92007, JIC C 8912, and ASTM E927-05.

External Quantum Efficiency: The EQE system (Newport MKS, USA) was composed of a quartz tungsten halogen (QTH) light source (250 W), a chopper set to 30 Hz, a filter wheel with filters at 320, 570, and 860 nm, a CS260 monochromator, and SR810 lock-in amplifier with a preamplifier connected to the device. The scan was set to a spectrum range of 300–950 nm.

Charge Extraction: The measurements were performed using Autolab Potentiostat-Galvanostat (PGSTAT) with a FRA32M LED driver equipped with a white light source when the illumination was from the back (glass) side. The measurements were taken in Nova 1.1 software program to collect and analyze the data. The first step was identical to the voltage decay measurements. In the second step, the light was shut down and the system waited for certain time (delay time) before reconnecting and collecting the remained charges. The measurement had several cycles wherein each cycle had a different delay time between 0.5 and 20 s.

Supporting Information

Supporting Information is available from the Wiley Online Library or from the author.

Acknowledgements

The authors would like to thank the Israel Science Foundation (grant number 937/18) and the Ministry of Energy for their financial support of this work. The authors would like to express their very great appreciation to Dr. Inna Popov for her valuable and constructive calculation of excitation volume simulation.

Conflict of Interest

The authors declare no conflict of interest.

Data Availability Statement

The data that support the findings of this study are available from the corresponding author upon reasonable request.

Keywords

electron transport layers, hole transport layers, inverted structures, selective contacts

Received: July 26, 2021

Revised: October 1, 2021

Published online:

- [1] NREL, Best Research-Cell Efficiency Chart | Photovoltaic Research | NREL <https://www.nrel.gov/pv/cell-efficiency.html> (accessed: June 2019).
- [2] Y. Huang, X. Lei, T. He, Y. Jiang, M. Yuan, *Adv. Energy Mater.* **2021**, 2100690.
- [3] A. Y. Alsalloum, B. Turedi, K. Almasabi, X. Zheng, R. Naphade, S. D. Stranks, O. F. Mohammed, O. M. Bakr, *Energy Environ. Sci.* **2021**, 14, 2263.
- [4] H. S. Kim, C. R. Lee, J. H. Im, K. B. Lee, T. Moehl, A. Marchioro, S. J. Moon, R. Humphry-Baker, J. H. Yum, J. E. Moser, M. Grätzel, N.-G. Park, *Sci. Rep.* **2012**, 2, 591.
- [5] Y. Jiang, E. J. Juarez-Perez, Q. Ge, S. Wang, M. R. Leyden, L. K. Ono, S. R. Raga, J. Hu, Y. Qi, *Mater. Horizons* **2016**, 3, 548.
- [6] Y. Wang, Y. Liang, W. Yang, L. Sun, D. Xu, *Adv. Funct. Mater.* **2018**, 28, 1801237.
- [7] T. Ishihara, *J. Lumin.* **1994**, 60–61, 269.
- [8] W. Ning, F. Wang, B. Wu, J. Lu, Z. Yan, X. Liu, Y. Tao, J.-M. M. Liu, W. Huang, M. Fahlman, L. Hultman, *Adv. Mater.* **2018**, 30, 1706246.
- [9] M. F. Mohamad Noh, C. H. The, R. Daik, E. L. Lim, C. C. Yap, M. A. Ibrahim, N. Ahmad Ludin, A. R. B. Mohd Yusoff, J. Jang, M. A. Mat Teridi, *J. Mater. Chem. C*, **2018**, 6, 682.
- [10] I. Hussain, H. P. Tran, J. Jaksik, J. Moore, N. Islam, M. J. Uddin, *Emergent Mater.* **2018**, 1, 133.
- [11] X. Yin, J. Zhai, T. Wang, W. Jing, L. Song, J. Xiong, F. Ko, *ACS Appl. Mater. Interfaces* **2019**, 11, 12460.
- [12] P. Docampo, J. M. Ball, M. Darwich, G. E. Eperon, H. J. Snaith, *Nat. Commun.* **2013**, 4, 1.
- [13] C. G. Wu, C. H. Chiang, Z. L. Tseng, M. K. Nazeeruddin, A. Hagfeldt, M. Grätzel, *Energy Environ. Sci.* **2015**, 8, 2725.
- [14] C. Y. Xu, W. Hu, G. Wang, L. Niu, A. M. Elseman, L. Liao, Y. Yao, G. Xu, L. Luo, D. Liu, Guangdong Zhou, Ping Li, Qunliang Song, *ACS Nano* **2020**, 14, 196.
- [15] Y. Li, Z. Xu, S. Zhao, D. Song, B. Qiao, Y. Zhu, J. Meng, *Molecules* **2019**, 24, 2027.
- [16] C. H. Chiang, J. W. Lin, C. G. Wu, *J. Mater. Chem. A* **2016**, 4, 13525.
- [17] L. Etgar, P. Gao, Z. Xue, Q. Peng, A. K. Chandiran, B. Liu, M. K. Nazeeruddin, M. Grätzel, *J. Am. Chem. Soc.* **2012**, 134, 17396.
- [18] W. Kong, W. Li, C. Liu, H. Liu, J. Miao, W. Wang, S. Chen, M. Hu, D. Li, A. Amini, Yang, S. *ACS Nano* **2019**, 13, 1625.
- [19] Y. Huang, T. Liu, C. Liang, J. Xia, D. Li, H. Zhang, A. Amini, G. Xing, C. Cheng, *Adv. Funct. Mater.* **2020**, 30, 2000863.
- [20] P. Cui, D. Wei, J. Ji, D. Song, Y. Li, X. Liu, J. Huang, T. Wang, J. You, M. Li, *Sol. RRL* **2017**, 1, 1600027.
- [21] H. Yu, J. Ryu, J. W. Lee, J. Roh, K. Lee, J. Yun, J. Lee, Y. K. Kim, D. Hwang, J. Kang, Kim, S. K., *ACS Appl. Mater. Interfaces* **2017**, 9, 8113.
- [22] J. F. Liao, W. Q. Wu, Y. Jiang, D. Kuang, Bin, L. Wang, *Sol. RRL* **2019**, 3, 1800268.
- [23] Z. Xiao, Y. Yuan, Y. Shao, Q. Wang, Q. Dong, C. Bi, P. Sharma, A. Gruverman, J. Huang, *Nat. Mater.* **2015**, 14, 193.
- [24] G. Abdelmageed, L. Jewell, K. Hellier, L. Seymour, B. Luo, F. Bridges, J. Z. Zhang, S. Carter, *Appl. Phys. Lett.* **2016**, 109, 233905.

- [25] C. C. Boyd, R. Cheacharoen, T. Leijtens, M. D. McGehee, *Chem. Rev.* **2019**, pp 3418.
- [26] L. Huang, D. Zhang, S. Bu, R. Peng, Q. Wei, Z. Ge, *Adv. Sci.* **2020**, 7, 1902656.
- [27] P. Zhao, B. J. Kim, H. S. Jung, *Mater. Today Energy*, **2018**, pp 267.
- [28] G. Boschloo, D. Fitzmaurice, *J. Phys. Chem. B* **1999**, 103, 2228.
- [29] Y. Li, Y. Zhao, Q. Chen, Y. M. Yang, Y. Liu, Z. Hong, Z. Liu, Y. T. Hsieh, L. Meng, Y. Li, Y. Yang, *J. Am. Chem. Soc.* **2015**, 137, 15540.
- [30] H. Kim, Bin, I. Im, Y. Yoon, S. Do Sung, E. Kim, J. Kim, W. I. Lee, *J. Mater. Chem. A* **2015**, 3, 9264.
- [31] H. Nagaoka, F. Ma, D. W. Dequillettes, S. M. Vorpahl, M. S. Glaz, A. E. Colbert, M. E. Ziffer, D. S. Ginger, *J. Phys. Chem. Lett.* **2015**, 6, 669.
- [32] S. Rahmany, L. Etgar, *Mater. Adv.* **2021**, 2, 2617.
- [33] S. Singh, B. Sharma, G. Banappanavar, A. Dey, S. Chakraborty, K. L. Narasimhan, P. Bhargava, D. Kabra, *ACS Appl. Energy Mater.* **2018**, 1, 1870.
- [34] N. Shibayama, H. Kanda, T. W. Kim, H. Segawa, S. Ito, *APL Mater.* **2019**, 7, 31117.
- [35] M. C. Brennan, S. Draguta, P. Kamat, V., M. Kuno, *ACS Energy Lett.* **2018**, 3, 204.
- [36] Q. Jiang, Z. Chu, P. Wang, X. Yang, H. Liu, Y. Wang, Z. Yin, J. Wu, X. Zhang, J. You, *Adv. Mater.* **2017**, 29, 1703852.
- [37] V. Thacker, V., L. O. Herrmann, D. O. Sigle, T. Zhang, T. Liedl, J. J. Baumberg, U. F. Keyser, *Nat. Commun.* **2014**, 5, 1.
- [38] F. Zabihi, Y. Xie, S. Gao, M. Eslamian, *Appl. Surf. Sci.* **2015**, 338, 163.
- [39] J. H. Kuang, H. L. Chien, *Adv. Sci. Lett.* **2011**, 4, 3570.
- [40] M. Pylnev, A. M. Barbisan, T. C. Wei, *Appl. Surf. Sci.* **2021**, 541, 148559.
- [41] N. Rolston, K. A. Bush, A. D. Printz, A. Gold-Parker, Y. Ding, M. F. Toney, M. D. McGehee, R. H. Dauskardt, *Adv. Energy Mater.* **2018**, 8, 1802139.
- [42] A. Efrati, S. Aharon, M. Wierzbowska, L. Etgar, *EcoMat* **2020**, 2, 1.
- [43] M. Becker, M. Wark, *Org. Electron.* **2017**, 50, 87.
- [44] M. Cai, N. Ishida, X. Li, X. Yang, T. Noda, Y. Wu, F. Xie, H. Naito, D. Fujita, L. Han, *Joule* **2018**, 2, 296.
- [45] P.-H. Huang, Y.-H. Wang, C.-W. Huang, W.-R. Chen, C.-J. Huang, *Crystals* **2018**, 8, 358.
- [46] C. C. Chen, S. H. Bae, W. H. Chang, Z. Hong, G. Li, Q. Chen, H. Zhou, Y. Yang, *Mater. Horizons* **2015**, 2, 203.
- [47] W. Tress, J. P. Correa Baena, M. Saliba, A. Abate, M. Graetzel, *Adv. Energy Mater.* **2016**, 6, 1600396.
- [48] I. Zarazua, G. Han, P. P. Boix, S. Mhaisalkar, F. Fabregat-Santiago, I. Mora-Seró, J. Bisquert, G. Garcia-Belmonte, *J. Phys. Chem. Lett.* **2016**, 7, 5105.
- [49] J. H. Heo, H. J. Han, D. Kim, T. K. Ahn, S. H. Im, *Energy Environ. Sci.* **2015**, 8, 1602.
- [50] Z. Zhu, J. Ma, Z. Wang, C. Mu, Z. Fan, L. Du, Y. Bai, L. Fan, H. Yan, D. L. Phillips, S. Yang, *J. Am. Chem. Soc.* **2014**, 136, 3760.
- [51] B. Cohen, El, S. Aharon, A. Dymshits, L. Etgar, *J. Phys. Chem. C* **2016**, 120, 142.
- [52] L. Dou, Y. M. Yang, J. You, Z. Hong, W. H. Chang, G. Li, Y. Yang, *Nat. Commun.* **2014**, 5, 1.
- [53] R. A. Belisle, W. H. Nguyen, A. R. Bowring, P. Calado, X. Li, S. J. C. Irvine, M. D. McGehee, P. R. F. Barnes, B. C. O'Regan, *Energy Environ. Sci.* **2017**, 10, 192.
- [54] W. Tress, M. Yavari, K. Domanski, P. Yadav, B. Niesen, J. P. Correa Baena, A. Hagfeldt, M. Graetzel, *Energy Environ. Sci.* **2018**, 11, 151.